New Journal of Physics
The open access journal at the forefront of physics

Deutsche Physikalische Gesellschaft DPG IOP Institute of Physics

PAPER • OPEN ACCESS

4D texture of circular dichroism in soft-x-ray photoemission from tungsten

To cite this article: O Fedchenko *et al* 2019 *New J. Phys.* **21** 013017

View the article online for updates and enhancements.

IOP ebooks™

Bringing you innovative digital publishing with leading voices to create your essential collection of books in STEM research.

Start exploring the collection - download the first chapter of every title for free.

This content was downloaded from IP address 80.209.204.211 on 21/01/2019 at 07:31

New Journal of Physics
The open access journal at the forefront of physics

Deutsche Physikalische Gesellschaft DPG
IOP Institute of Physics

Published in partnership with: Deutsche Physikalische Gesellschaft and the Institute of Physics

OPEN ACCESS

RECEIVED
28 August 2018

REVISED
13 November 2018

ACCEPTED FOR PUBLICATION
29 November 2018

PUBLISHED
18 January 2019

Original content from this work may be used under the terms of the Creative Commons Attribution 3.0 licence.

Any further distribution of this work must maintain attribution to the author(s) and the title of the work, journal citation and DOI.

PAPER

4D texture of circular dichroism in soft-x-ray photoemission from tungsten

O Fedchenko[1], K Medjanik[1], S Chernov[1], D Kutnyakhov[1,6], M Ellguth[1,2], A Oelsner[2], B Schönhense[3], T R F Peixoto[4], P Lutz[4], C-H Min[4], F Reinert[4], S Däster[5], Y Acremann[5], J Viefhaus[6], W Wurth[6,7], J Braun[8], J Minár[9], H Ebert[8], H J Elmers[1] and G Schönhense[1,10]

[1] Institut für Physik, Johannes Gutenberg-Universität Mainz, Germany
[2] Surface Concept GmbH, Mainz, Germany
[3] Dept. of Bioengineering, Imperial College, London, United Kingdom
[4] Universität Würzburg, Experimentelle Physik VII, 97074 Würzburg, Germany
[5] Laboratorium für Festkörperphysik, ETH Zürich, Switzerland
[6] DESY, Hamburg, Germany
[7] CFEL, Universität Hamburg, Germany
[8] Dep. Chemie und Biochemie, Ludwig-Maximilians-Universität, München, Germany
[9] New Technologies Research Centre, University of West Bohemia, Plzeň, Czechia
[10] Authors to whom any correspondence should be addressed.

E-mail: schoenhe@uni-mainz.de

Keywords: photoemission, soft x-rays, circular dichroism, W(110), ToF momentum microscopy

Supplementary material for this article is available online

Abstract

Photoemission-intensity distributions $I_{RCP/LCP}(E_B, \boldsymbol{k})$ measured for right- and left-circularly polarized soft x-rays revealed a large circular dichroism in angular distribution (*CDAD*) in the 4D parameter space (E_B binding energy, $\boldsymbol{k}$ momentum vector). Full-field *k*-imaging combined with time-of-flight energy recording at a high-brilliance soft x-ray beamline allowed mapping the *CDAD* in the bulk Brillouin zone of tungsten and the entire *d*-band complex within a few hours. *CDAD*-asymmetries are very high (up to 90%), persist throughout the whole photon-energy range (300–1300 eV) and show a pronounced dependence on momentum $\boldsymbol{k}$ and binding energy E_B, visualized as movies or sequences of cuts through the 4D object. One-step photoemission calculations for the same photon energies show fair agreement with the measured results. In addition to the requirement of a 'handed' experimental geometry, known from previous experiments on adsorbates and surface states, we find an anti-symmetric behavior of the *CDAD* with respect to two bulk mirror planes. A new symmetry condition along the perpendicular momentum k_z makes *CDAD* a valuable tool for an unambiguous identification of high-symmetry planes in direct transitions in the periodic zone scheme. Technically, the method provides a circular polarimeter for soft, tender and hard x-rays.

1. Introduction

A system exhibits circular or linear dichroism if it responds differently to photon beams of two orthogonal polarization states [1]. Pioneering work on magnetic materials by Schütz *et al* [2], Thole and van der Laan [3], Stöhr [4] and others initiated intensive research, and today, *x-ray magnetic circular dichroism* (XMCD) is a common tool in the field of magnetism. Ritchie [5], Cherepkov [6], and Lee [7] generalized the phenomenon of dichroism to angular-resolved photoemission and termed it *circular (or linear) dichroism in the angular distribution (CDAD* or *LDAD)*. At first, the studied objects were mostly oriented molecules and adsorbate systems [8], while later it was proven that photoemission from non-magnetic solids in fact also yields sizeable *CDAD* asymmetries in angular-resolved observation [9–12]. A necessary precondition is a definite handedness in the photoemission geometry [13]. This requirement can be fulfilled for band states as well. From a quasi-atomic perspective, *CDAD* and *LDAD* are determined by the interference of different outgoing partial waves

© 2019 The Author(s). Published by IOP Publishing Ltd on behalf of Deutsche Physikalische Gesellschaft

being sensitive to their phase-shift differences. The differential photoemission cross section is proportional to the squared total dipole matrix element that contains interference terms between different final-state partial waves. Upon reversal of the photon helicity (in case of *CDAD*) or switching of the electric vector between orthogonal directions (for *LDAD*), interference terms with odd symmetry change their signs. This is the origin of the dichroism in the photoelectron angular distribution. This phenomenon exists in the pure electric dipole approximation and thus it differs from the 'natural' CD of chiral molecules, which is described by higher-order terms in the electron-photon operator [14].

In the present work we employ the technique of time-of-flight (ToF) *k*-microscopy for a comprehensive study of the *CDAD* in the soft-x-ray spectral range. This new method captures simultaneously more than one full Brillouin zone (BZ) for binding energies in a range of several eV, yielding full information from the valence bands. In the vacuum ultraviolet (VUV) range, this instrument was previously used for the study of *LDAD* in photoemission from Mo(110) surface states and surface resonances [15]. These states are characterized by their 2D character and their location at the surface, wherefore they fulfill the criteria discussed for adsorbate systems [13]. Earlier work on graphite [16] and Pd [17] revealed that a *CDAD* also exists in photoemission from crystalline samples. However, the low photon energies used essentially probe the surface character of the bands. Hence, these results cannot be considered representative for true 3D bulk states. Moreover, no information on the dependence of the *CDAD* on the electron-momentum component perpendicular to the sample surface could be extracted from these low-energy data.

CDAD has previously been observed in the soft-x-ray range for spherically-symmetric initial states as a consequence of dissymmetry in the final state [18, 19]. Fecher [20] proved that the existence of the (partially-reflecting) surface barrier alone is a sufficient condition for appearance of *CDAD* in photoemission from a spherically-symmetric initial state, e.g. a 1s core level in the topmost layer. This work was the first hint on the importance of photoelectron diffraction on the *CDAD*. Reference [21] outlines how the radial matrix elements and relative phase shift could be determined in photoemission to identify the differential cross section.

Previous experiments in the soft [22–24] and hard x-ray range [25, 26] showed band dispersion in photoemission at higher photon energies. This fact indicated that direct interband transitions prevail. Such transitions are *umklapp*-processes, i.e. a reciprocal lattice vector is involved in order to fulfill energy and momentum conservation simultaneously [27, 28].

Here, we investigate the *CDAD* for valence bands in the bulk of a material. We have chosen tungsten because it is known that due to the high Debye temperature the band features persist up to high photon energies [25]. In order to scan the momentum component perpendicular to the surface, we used soft-x-ray excitation at various photon energies between 300 and 1300 eV. An *ab initio* calculation using the one-step model was performed for the same photon energies. The main goal was to elucidate whether a *CDAD* exists for bulk bands with negligible surface contribution and whether the basic concept of the origin of *CDAD* in direct inter-band transitions is still valid in the x-ray range. A crucial point is that the phase-shift differences, playing a central role in *CDAD* at low energies [13], tend to zero with increasing photon energies [29]. Experimentally, both photon helicities have been measured separately and in the derivation of *CDAD* no symmetry properties have been exploited because it was not *a-priori* clear which of them would persist when the photon momentum is non-negligible. High asymmetries up to 90% make *CDAD*-spectroscopy a powerful circular polarimeter in a huge photon-energy range from the VUV up to the hard x-ray range (see also note added in proof).

2. Theory

2.1. Quantum-mechanical nature of the CDAD

In order to understand the origin of the dichroism asymmetries in the observed patterns, we start with a review of its quantum-mechanical nature. The *CDAD* maps are determined as differences of intensity data sets $I_{\mathrm{RCP,LCP}}(E_\mathrm{B}, \boldsymbol{k})$ taken for right and left circular polarizations (RCP and LCP, respectively). The difference $I_\mathrm{RCP} - I_\mathrm{LCP}$ yields the *CDAD signal*, whereas division by the *sum* $I = I_\mathrm{RCP} + I_\mathrm{LCP}$ gives the *CDAD asymmetry* (in analogy to the definitions of the magnetic circular dichroism [2–4]).

The symmetrized intensity, where the *CDAD* contribution is eliminated (all *CDAD* terms cancel each other) and the two quantities characterizing the dichroism (*CDAD signal and asymmetry*) are thus derived according to

$$\begin{aligned} I(E_\mathrm{B}, \mathbf{k}) &= I_\mathrm{RCP}(E_\mathrm{B}, \mathbf{k}) + I_\mathrm{LCP}(E_\mathrm{B}, \mathbf{k}), \\ CDAD(E_\mathrm{B}, \mathbf{k}) &= I_\mathrm{RCP}(E_\mathrm{B}, \mathbf{k}) - I_\mathrm{LCP}(E_\mathrm{B}, \mathbf{k}), \\ A_{CDAD}(E_\mathrm{B}, \mathbf{k}) &= CDAD(E_\mathrm{B}, \mathbf{k})/I(E_\mathrm{B}, \mathbf{k}). \end{aligned} \tag{1}$$

In comparison with previous work on oriented molecules or adsorbates, the symmetrized intensity array $I(E_\mathrm{B}, \boldsymbol{k})$ represents the differential cross section for excitation with unpolarized light $\left(\frac{\mathrm{d}\sigma}{\mathrm{d}\Omega}\right)_\mathrm{unpol}$, except for a factor of 2. Then, *CDAD* can be understood as the difference between the cross sections for excitation with RCP

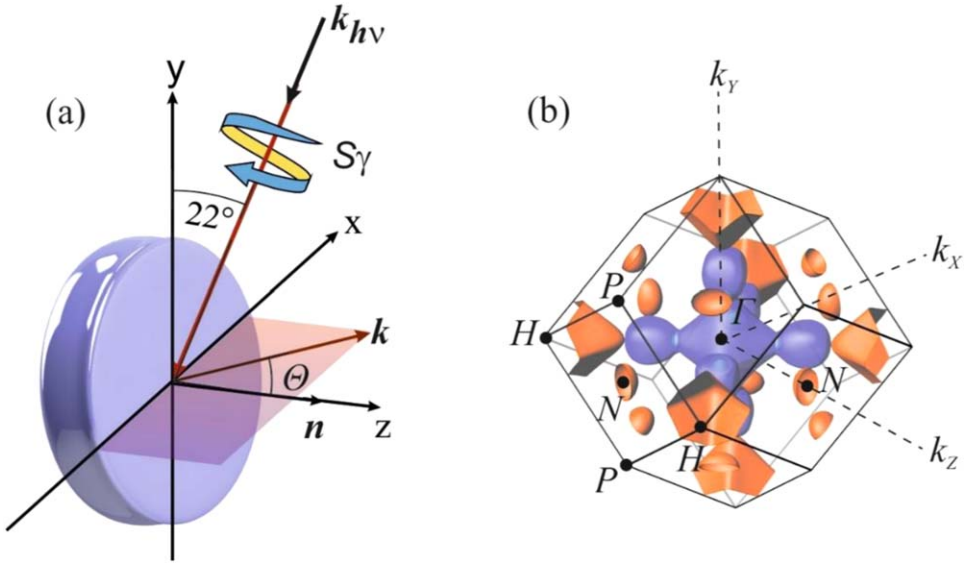

Figure 1. Schematic view of the experimental geometry in real space (a) and corresponding bulk Brillouin zone of W in *k*-space (b) [31, 32]. In the latter, red and blue colors denote hole and electron conductivity features, respectively. Photon-helicity vector $\boldsymbol{S}_\gamma$, photoelectron momentum $\boldsymbol{k}$ and surface normal $\boldsymbol{n}$ (along the *z* axis) induce a handedness. The incoming photon beam lies in the *y*–*z* plane, 22° to the *y*-axis. The momentum distributions for both photon helicities were taken for a field-of-view with radius $k_{||} \sim 2$ Å^{-1}, exceeding the size of the Brillouin zone.

and LCP light. $A_{CDAD}(E_B, \boldsymbol{k})$ varies between +100% and −100% and is thus used for a quantification of the *CDAD* effect.

As the basis for the interpretation of the results, we recall the essentials of dichroism effects in photoemission from earlier work [5–9, 18–21, 30]. Experimentally, *CDAD* for non-magnetic systems is observed for a dissymmetric (handed) spatial arrangement of the quantization axis of initial state orbital momenta ($\boldsymbol{n}$), the photon impact direction ($\boldsymbol{k_{h\nu}}$) and the photoelectron momentum ($\boldsymbol{k_e}$) (see figure 1(a)). In other words, *CDAD* from non-magnetic targets requires a handedness in the experimental geometry.

For the results shown below, the plane of incidence coincides with the crystallographic *Γ*–*H*–*N* plane (k_y–k_z) of the sample, as sketched in figure 1(b). For RCP and LCP light, the in-plane (E_y) and out-of-plane component (E_z) of the electric vector have a phase-shift difference of $\pm\pi/2$. Because the total system of sample plus photon beam is no longer invariant under the mirror operation parallel to *Γ*–*H*–*N*, the preconditions for *CDAD* are fulfilled. Due to the shallow incidence, the (relative) *y*- and *z*-components of the electric vector are given by $\sin(22°) \approx 0.37$ and $\sin(68°) \approx 0.92$, respectively. Taking into account these projections, the photon operator can be written as $0.92z - 0.37y + ix$ for RCP light and $0.92z - 0.37y - ix$ for LCP light. We note that the index of refraction is ~0.98 in the photon energy range used so that the Fresnel equations do not play a role.

We can already derive some general conclusions for this experimental geometry: the axial photon-helicity vector $\boldsymbol{S}_\gamma$ breaks the symmetry of the *y*–*z* plane. Hence, according to the main criteria for the appearance of *CDAD* the asymmetry should thus be anti-symmetric with respect to the *y*–*z* plane and vanish for $k_X = 0$ (see also equation (1)). Even in the unpolarized case, the photon beam itself (i.e. the vector $\boldsymbol{k_{h\nu}}$) breaks the mirror symmetry with respect to the *x*–*z* plane. Hence the *CDAD* patterns will not be symmetric with respect to the horizontal mirror plane of the crystal. In particular, the effect of the photon momentum will show up in a dissymmetry with respect to the horizontal plane, as we will see in section 4.

As a simple example, we consider the allowed dipole transitions for the case of an initial band with pure d_{z^2}-symmetry. The selection rules for a dipole photo-transition lead to *p* and *f* final-state partial waves. The differential photoemission cross section is given by Fermi's Golden Rule taking into account the proper angular wave functions [33]. For the atomic-like d_{z^2}-orbital (Y_{20}) we have $d\sigma/d\Omega \propto |\langle \Psi_{fin} | 0.92z - 0.37y \pm ix | d_{z^2} \rangle|^2$. Each of the three terms of the dipole operator excites a *p*- and a *f*-wave, as sketched figures 2(b)–(m). By switching the photon helicity, two of the final-state partial waves change their relative phases by π as marked by the color (see figures 2(f), (g), (l), (m)). Since the total final state is the coherent superposition of all allowed partial waves, this phase jump shows up in the differential cross sections for circularly polarized light: the complete angular distribution is rotated clockwise for the RCP dipole operator and counterclockwise for the LCP operator, see figures 2(n), (o). The size of this rotation depends on the relative phases of the interfering partial waves. The interference behavior in the atomic-like and adsorbate case is discussed in detail in [13, 34]. In

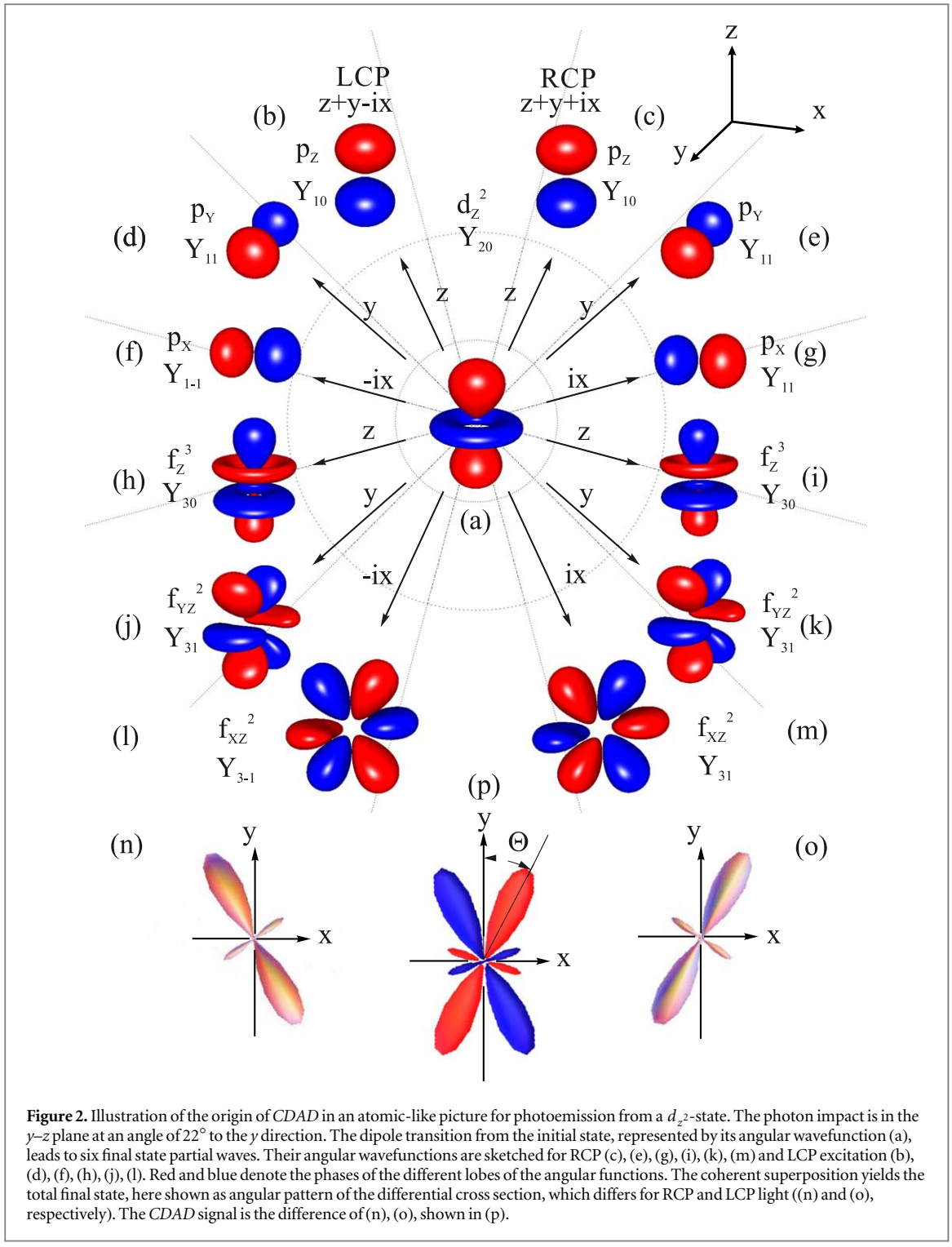

Figure 2. Illustration of the origin of *CDAD* in an atomic-like picture for photoemission from a d_{z^2}-state. The photon impact is in the *y*–*z* plane at an angle of 22° to the *y* direction. The dipole transition from the initial state, represented by its angular wavefunction (a), leads to six final state partial waves. Their angular wavefunctions are sketched for RCP (c), (e), (g), (i), (k), (m) and LCP excitation (b), (d), (f), (h), (j), (l). Red and blue denote the phases of the different lobes of the angular functions. The coherent superposition yields the total final state, here shown as angular pattern of the differential cross section, which differs for RCP and LCP light ((n) and (o), respectively). The *CDAD* signal is the difference of (n), (o), shown in (p).

bulk photoemission as discussed here, additional phase differences of partial waves arise due to diffraction of the photoelectron wave on neighboring atoms.

This rotation of the differential cross section depending on the photon helicity, a consequence of the phase jump in one or several partial waves, is the basic mechanism that generates the *CDAD* signal (figure 2(p)). The figure makes clear that the dichroism on the one hand reflects the *symmetry properties and orientation of the initial-state* and on the other hand the *partial-wave composition of the final-state*, including their symmetry behavior with respect to reversal of the photon helicity. For the band states studied below, the situation is more complex because the symmetry-adapted initial eigen-states of the solid can be described as an appropriate linear combination of many partial waves characterized by the quantum numbers ***l*** and ***m*** (according to the involved spherical harmonics) [35].

Due to the finite grazing-incidence angle of 22° this geometry also gives rise to a (generally small) contribution of the *LDAD*. It will show up in terms of an 'up–down' dissymmetry, even when the *x*–*z* plane is a mirror plane, see figure 1(a).

2.2. Calculations within the one-step model

Calculations complementary to the experiment were made on the base of recent developments of the one-step model of photoemission in which all spin–orbit effects are accounted for [36]. For photon energies in the soft-x-ray range the photon momentum reaches values of 0.7 $Å^{-1}$ causing significant changes in the photoelectron distributions. To account for this, the calculations included the photon momentum within the description of the photo excitation. The conservation of momentum causes a rigid shift (in $k_{||}$ and $k_{\perp}$) of the spectral intensity distributions in *k*-space along the direction of the incoming photon beam, as visualized for example in figure 5. The shift is less pronounced for photon energies in the range of 400 eV but it appears significantly with values of about 0.5 $k_{||}$ for x-ray photon energies of 1 keV. The present approach accounts for electronic correlations within the local density approximation (LDA) and can be applied to the electronic structure of 3D- and 2D-systems. The formalism includes matrix-element effects which modify the bare spectral function, as well as multiple-scattering processes of the photoelectron in a large spectral range from 10 eV to 10 keV.

Recently, calculations of angle-resolved photoemission within the one-step model have been extended to the high-energy regime that probes primarily the bulk electronic structure. However, in all energy regimes it is necessary to account properly for the wave-vector and energy dependence of the transition matrix elements. These dependences must not be neglected, because they are the result of strong multiple-scattering processes and also include the effects of selection rules [37]. Venturini *et al* [10] investigated the band mapping potential of angle-resolved photoemission spectroscopy in the soft-x-ray range for the Ag(001) surface. Calculations and experimental results showed that the photon momentum has an impact already on the band mapping at soft-x-ray energies. A similar experiment was performed for W(110) and band features were observed in photoemission up to 870 eV [38]. At higher photon energies, ranging from 1 up to 10 keV, a new approach for the final state has been applied, which generalized the single-scattering approach. Good agreement between result based on this approach and the experiment was found for clean Fe(001) and MgO/Fe(100). Since the *CDAD* depends crucially on matrix elements and partial wave phases, it provides an ideal testing ground for new theoretical approaches for spectroscopic calculations.

The initial band state is a symmetry-adapted eigenstate of the crystal and can be described as a Bloch wave. For high photon energies the final state is considered to be a free-electron-like plane wave [27, 28] with increasingly shorter wavelength for increasing excitation energies. At kinetic energies between 300 and 1300 eV the wavelength of the final state wave function varies between $\lambda \approx 4$ and 1 Å. The oscillations of the final-state wave function on the atomic length scale cause substantial changes in the radial integrals of the dipole matrix element. It is the purpose of the present paper to elucidate the validity of the model of direct interband transitions for the interpretation of photoemission dynamics in a wide energy range between $h\nu = 300$ and 1300 eV. As a sensitive probe for matrix elements and relative phases of partial waves, we employ *CDAD* measurements for tungsten for the complete surface BZ and full energy range of the *d*-bands.

Our present theoretical approach for the final state is limited to photon energies where dipole transitions prevail. In the tender and hard x-ray range quadrupole transitions become increasingly significant. Also the neglect of multiple-scattering effects for the final state within the atomic layers works quantitatively only for photon energies above some hundred eV. For typical angular-resolved photoelectron spectroscopy (ARPES) energies ranging from 10 to 150 eV one has to consider these multiple scattering effects, where a spherical wave expansion up to $l_{max} = 7$ or 8 has to be applied, as known from LEED calculations. Furthermore, we had to use 80–100 two-dimensional reciprocal lattice vectors in the calculation of the corresponding layer scattering matrices for the soft x-ray photon energies used in the measurements. In typical ARPES calculations the use of 20–40 reciprocal lattice vectors is sufficient for a quantitative spectroscopic analysis. This is due to back-folding effects from higher 2D BZs which modify the corresponding spectral intensities in the soft x-ray photon energy range.

Figure 3 shows calculated constant-energy sections in the photon energy range from 1270 to 1380 eV. The sections show the sum of the intensities calculated for left and right circular polarization. The direction of the incident light has been chosen according to the experimental set-up (from top to bottom). In this photon energy range the probed perpendicular momentum component k_z does not depend much on the parallel component. Assuming a free-electron-like final state the photon energy range corresponds to k_z values between 6.5 G_{110} and 6.76 G_{110} (G_{110} being the reciprocal lattice vector perpendicular to the ⟨110⟩-surface), thus covering a quarter of the seventh repeated BZ along k_z. The constant-energy section at $k_z = 6.5\ G_{110}$ (figure 3(a)) corresponds to a cut through the Fermi surface in the *N*–*H*–*P* plane. Here, the high-symmetry points *N* and *H* coincide with the high-symmetry points in the two-dimensional surface BZ $\overline{\Gamma}$ and $\overline{N}$, respectively, labeled in panel (g). The latter are

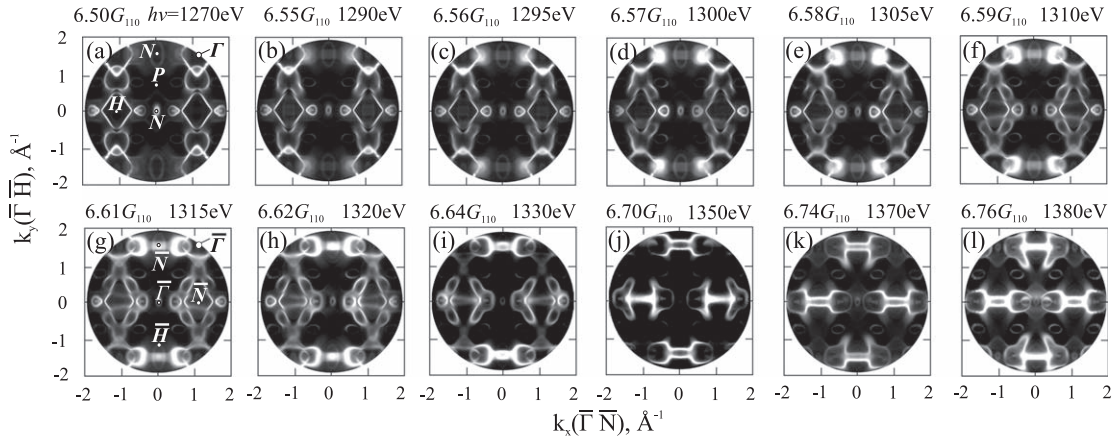

Figure 3. Calculated constant-energy sections of the photoemission intensity at the Fermi energy as function of photon energy. The momentum perpendicular to the surface is quantified in multiples of the reciprocal lattice vector G_{110}. Note the significant changes for increments as small as 0.01 Å^{-1}. Effective mass and inner potential were $m_{\rm eff}/m = 1.033$ and $V_0^* = 10$ eV (referenced to $E_{\rm F}$). High-symmetry points are denoted in (a) and (g) for the bulk and surface Brillouin zone, respectively.

valid independent on photon energy. Prominent features are the diamond-shaped rhombs centered at the *H*-points and at the *Γ*-points of the neighboring BZs (see figure 3(a)). Both rhombs shrink with increasing k_z revealing the dispersion with perpendicular momentum. In contrast the circularly shaped features near $(k_x, k_y) = (0.8, 1.4)$ Å^{-1} increase in size with increasing k_z. The ellipse at the *N*-point $(k_x, k_y) = (0, 1.4)$ Å^{-1} corresponds to a cut through the hole-like small ellipsoids centered at the *N*-points in 3D reciprocal space (see figure 1(b)). The strong k_z-dispersion of these features allows one to distinguish photon energy variations as small as 5 eV corresponding to a variation of $\Delta k_z = 0.01$ Å^{-1}. Surprisingly, some features remain constant in size with varying photon energy. This applies in particular to the central ring-shaped feature at the $\bar{\Gamma}$ point at $(k_x, k_y) = (0, 0)$ Å^{-1}. The k_z-independent behavior suggests that this state corresponds to a surface state resulting from the fact that the calculation considers a finite number of atomic layers. The intensity of the k_z-independent features increases on the expense of the dispersing states with decreasing photon energy.

In summary, the calculations predict sharp band features prevailing in photoemission with photon energies as high as 1380 eV. The band dispersion along k_z is surprisingly pronounced and well-resolved within increments as small as 0.01 Å^{-1}. Calculations with both photon helicities predict significant *CDAD* throughout the photon-energy range studied. The calculated *CDAD* texture will be compared with the experimental results, see figure 6.

3. Experimental

ARPES is the method of choice for the study of the electronic structure [27, 28]. Demanding a high energy resolution, ARPES is commonly performed in the VUV spectral region at photon energies <100 eV. In this energy range the inelastic mean free path (IMFP) of the photoelectrons is <0.5 nm, hence ARPES at those photon energies is ideally suited for the study of surface states and adsorbates. With increase of photoelectron kinetic energy towards the soft-x-ray range the IMFP increases from 0.5 nm at 200 eV to 2.5 nm at 2000 eV [39]. This implies that soft-x-ray ARPES gives access to deeper-lying layers of the solid. As a result, it is possible to probe the bulk electronic structure which is of interest e.g. in the context of transport properties.

Extending the well-established ARPES technique into the soft-x-ray range, we face obstacles concerning both excitation and detection. The required energy resolution (10 meV range) and momentum resolution (~1% of the size of the BZ) pose difficult challenges to the photon bandwidth ($\Delta E/E \approx 10^{-5}$) and angular resolution of the electron spectrometer (<0.1°). In addition, the photoemission cross section drops dramatically when going from the VUV to the soft-x-ray regime. Recently, several high-resolution synchrotron-radiation beamlines in the soft-x-ray range have become available. The low cross section and extremely high angular resolution needed for precise electronic band mapping at higher energies remain a challenge. Some pioneering experiments have been conducted so far [22–28, 40]. Due to the increased bulk sensitivity the problem of contamination during long acquisition times is less serious than at lower energies and even protective coatings were successfully used [22, 41].

In the present work, the intensity/resolution problem has been met by a conceptually new approach termed ToF momentum microscopy (for details, see [15, 42]). In contrast to conventional analyzers that work in terms

of angular coordinates, these electron microscopes directly image the (lateral) k_x- and k_y-coordinates in a large range of up to 4 Å^{-1} radius (for a new high-energy optics up to 10 Å^{-1} radius) . In the present work the kinetic energy is recorded in parallel via ToF detection. The maximum parallelization of data acquisition using this method relies on pulsed photon sources such as synchrotron radiation, high harmonic sources or laser radiation. In the determination of the spectral function $I(E_B, k_x, k_y)$ the usable energy width of a single measurement is limited to typically 6 eV by the chromatic aberration of the electron-optical system (for further details, see [43]). Acquiring ca. 10^6 data voxels simultaneously, the approach overcomes the intensity and k-resolution problem of ARPES in the soft-x-ray range.

All measurements shown below have been taken within ~5 h of beamtime at beamline P04 [44] of the storage ring PETRA III at DESY in Hamburg. The 40-bunch mode of PETRA III corresponds to a pulse period of 192 ns that perfectly matches 5 MHz count-rate capability of the delay-line detector. Thanks to the high parallelization, it was possible to run the experiment at the resolution limit of the beamline (i.e. 35 meV at $h\nu = 1$ keV). In the present work, data have been taken with circularly polarized light, reversing the photon helicity for each photon energy. This acquisition mode was different from our previous work on Mo(110) at low photon energies, where we exploited the dissymmetry induced by the tilted electric vector in order to obtain the *LDAD* asymmetry from a single run [15].

The momentum microscope uses the same imaging optics as described by Tusche *et al* [45], except that the dispersive analyzer is replaced by ToF energy detection. The optimized lens design developed in the Max Planck Institute in Halle, Germany, facilitated a k-resolution of 0.005 Å^{-1} [45]. Figure 1 in [42] shows the schematic cross section of the ToF k-microscope that relies on a general concept of optics. In the back focal plane of each objective lens, a Fourier image (reciprocal image) is formed. In the language of solid-state photoemission, this Fourier image represents the transversal momentum distribution of the photoelectrons. By adding the energy 'coordinate' via ToF recording, the present microscope acquires many 2D k_x–k_y-discs (exceeding the size of typical BZs) in parallel.

The electrostatic lens with a moderate immersion field (in the present experiment 8 kV across a gap of 4 mm) forms an achromatic momentum image in its backfocal plane, as originally exploited in LEEM [47, 48]. The subsequent lenses transfer a magnified k-image onto the detector. A size-selectable and adjustable field aperture in an intermediate real-space image plane facilitates the selection of well-defined source areas on the sample surface with diameters down to the micrometer range, without the need of an x-ray microfocus. A low-energy drift section serves as an energy-dispersive element. The time-resolving image detector of the delay-line type [46] acquires the (t, k_x, k_y) data sets.

Figure 1 shows the experimental geometry and defines the coordinate system. The circularly polarized x-ray beam was oriented at 22° to the y-axis. The tungsten crystal was prepared by repeated cycles of heating in oxygen (10^{-7} mbar, 1200 K) and short flashes (1900 K) in UHV. Prior to each measurement, the region of interest and position of the photon spot on the sample area was controlled using the real-space imaging mode of the microscope. This inspection made sure that no visible surface defects coincided with the region of interest, being defined by size and position of a field aperture [43]. For the present measurements, the field aperture was set to a circular acceptance range of 38 μm diameter on the sample surface, matching the footprint of the photon beam. The sample was mounted on a He-cooled hexapod manipulator for precise six-coordinates adjustment ($x, y, z, \theta_x, \theta_y, \phi$). All measurements have been performed at a sample temperature of 29 K.

4. Results

4.1. Direct transitions in 3D k-space observed by momentum microscopy

A graphical representation of a photo-transition in the bulk of a material is shown in figure 4(a). Analogously to the Ewald sphere in a diffraction experiment, the figure reflects energy conservation and the role of reciprocal lattice vectors in order to obey momentum conservation. For a given photon energy hν and binding energy E_B the final states of the photo-transition are located on a spherical shell with radius (for units Å^{-1} and eV):

$$k_f \sim 0.512\sqrt{h\nu - E_B + V_0^* \times \left(\frac{m_{\mathrm{eff}}}{m}\right)}. \quad (2)$$

$V_0{}^*$ is the inner potential that we refer to the Fermi energy, for convenience (note that the workfunction does not enter into equation (2)). m_{eff} and m are the effective mass of the electron in the final state inside the solid and the free-electron mass, respectively. The photon momentum $\boldsymbol{k}_{h\nu}$ is completely transferred to the photoelectron, leading to a rigid (vectorial) displacement of the final-state sphere. Given the impact angle of 22° (see figure 1), the displacements of the final-state sphere due to the photon momentum along k_z and k_y are

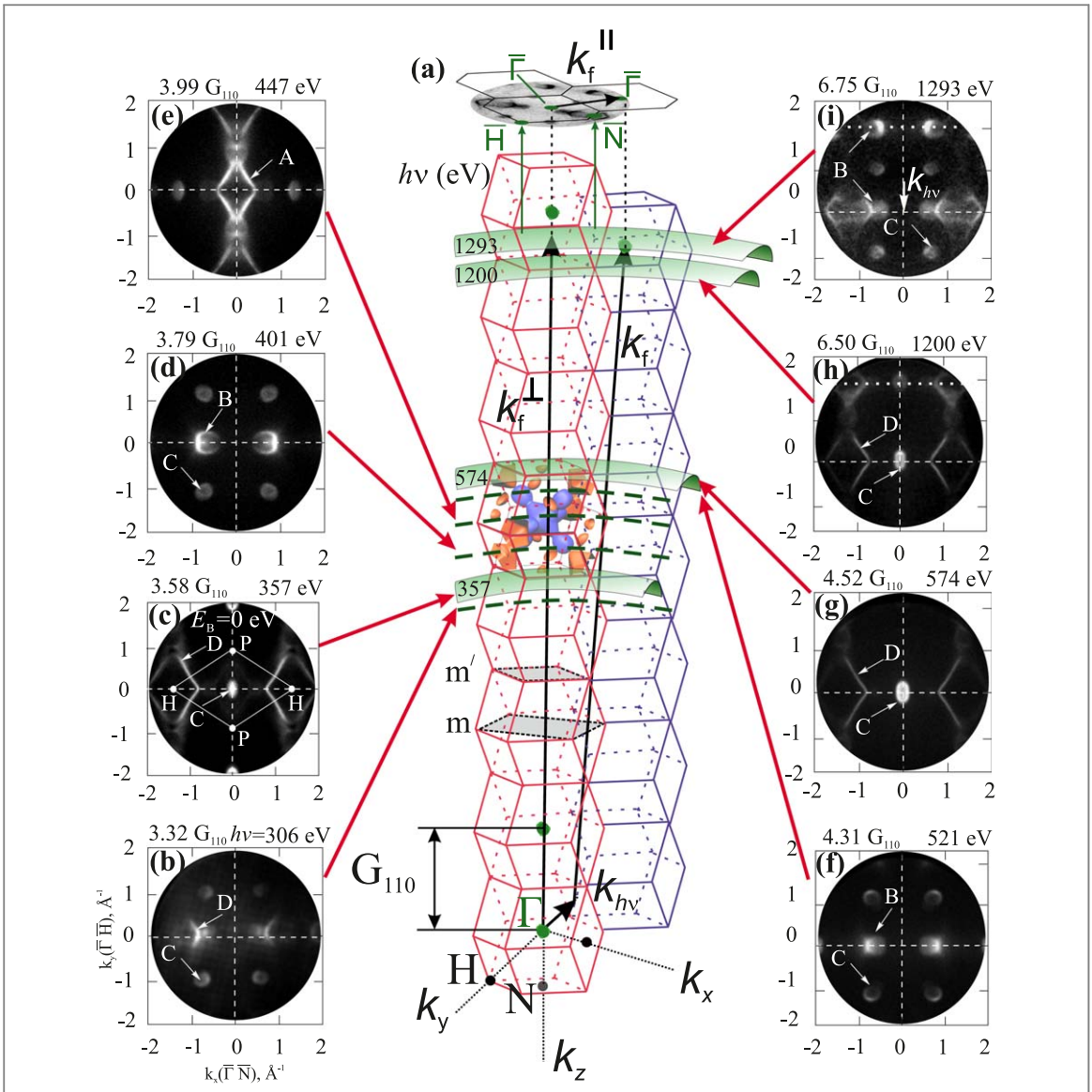

Figure 4. Periodic zone scheme for tungsten with direct transitions at various photon energies. The final states at a given energy lie on a spherical shell with radius given by the final-state electron momentum k_f (see equation (2)). The shell is rigidly displaced from the origin $\boldsymbol{k} = (0, 0, 0)$ by the vector of the photon momentum $\boldsymbol{k}_{h\nu}$. The perpendicular momentum component k_z has been quantified in multiples of the reciprocal lattice vector G_{110}. Size of the Brillouin zone and length of the momentum vectors are to scale. (b)–(i) Momentum sections at E_F for photon energies between 306 and 1293 eV as stated in the panels. The patterns are the sum of the measurements with RCP and LCP radiation.

$$\begin{aligned} \Delta k_z &= (2\pi\nu/c)\sin 22^\circ \\ \Delta k_y &= (2\pi\nu/c)\cos 22^\circ. \end{aligned} \tag{3}$$

For the highest photon energy used (1293 eV) we have $\Delta k_z = 0.237$ Å^{-1} and $\Delta k_y = 0.635$ Å^{-1}. Whereas the latter value shows up in terms of the rigid shift along negative k_y, the former reduces the value of k_z reached by the photo-transition. Referring to a free-electron like dispersion with adapted free electron mass, this acts like an apparent reduction of the photon energy by as much as 31 eV.

The kinetic energy of the emitted photoelectrons is selected by their ToF. The Fermi edge (high-energy cutoff of the spectral distributions) serves as reference for $E_B = 0$. Then the pattern observed on the detector represents the photoelectron intensity distribution as a function of the transversal momentum $\boldsymbol{k}_f^{\parallel}$ (disc at the top of figure 4(a)). The vector $\boldsymbol{k}_f^{\parallel}$ is conserved when the electrons leave the sample [47, 48], hence this method is characterized by a linear and achromatic momentum scale. The intensity of a transition is governed by Fermi's Golden Rule, containing the transition matrix elements and relative phases (see section 2.1). Figure 4 shows that the photon-energy range between 306 and 1293 eV corresponds to final states in the 3rd to 7th repeated BZ along the direction perpendicular to the surface (k_z). In all recorded patterns the strong surface resonance observed at low photon energies (see [42] and references therein) is completely absent. This proves that in this photon energy range the entire signal originates from bulk states.

The 4th repeated BZ has been mapped in a tomography-like manner by increasing the photon energy in small steps. For details of the data acquisition, see [40]. These individual 3D data stacks taken at different photon energies correspond to different values of k_z in the transition scheme. Figures 4(b)–(i) shows the momentum distributions (k_x–k_y sections) at the Fermi energy for eight selected photon energies. It is convenient to quantify the perpendicular component k_z in multiples of the reciprocal lattice vector along the $\langle 110 \rangle$-direction, $G_{110} = 2.812$ Å^{-1}. The in-plane projection of the photon momentum $\boldsymbol{k}_{h\nu}^{\parallel}$ points from top to bottom (see the arrow in figure 4(i)). The transfer of photon momentum thus leads to a rigid downward shift of the pattern, which increases linearly with photon energy. At 1293 eV this shift is sufficiently large that the Γ-point of the first repeated BZ in k_y-direction lies in the field of view (top dotted horizontal line in figure 4(i)). At the given photon flux there was a small but significant Lorentzian deformation of the Fermi-energy cutoff due to the space-charge effect, i.e. the repulsive Coulomb interaction between the large amount of slow secondary electrons and the fast photoelectrons. This Lorentzian deformation whose amplitude was between 0.5 and 1.5 eV for the measured data was removed by fitting a functional, as described in detail in [49]. After correcting for this space-charge effect, all 3D stacks are concatenated forming two 4D data arrays (one for each photon helicity), which contain the full information (except for the spin degree of freedom) on the electronic structure of the system that can be obtained by photoemission (see section 4.3).

The momentum sections at different photon energies in figure 4 reveal strong differences; see, e.g. the patterns at $h\nu = 357$ eV (with high-symmetry points indicated), 401 eV and 472 eV, corresponding to 3.58 G_{110}, 3.79 G_{110} and 4.10 G_{110}, (c), (d) and (e) respectively. The k_z-resolution is obviously very high so that the band features appear only when the spherical final-state shell intersects with the 'objects' in the BZ (i.e. Fermi-surface sheets and electron or hole pockets). Other patterns look very similar, e.g. those at 574 eV and 1200 eV (g), (h) are almost identical with the one at 357 eV (c). The only essential difference is a rigid downward shift with increasing energy, which is a fingerprint of the increasing transfer of photon momentum.

Inspection of the transition scheme reveals that these three sections lie very close to the *N*–*H*–*P* plane between adjacent BZs. Also, the patterns at the lowest (b) and highest photon energy (i) are quite similar except for the rigid shift, proving that in this range there is no significant deterioration of *k*-resolution and contrast with increasing photon energy. This similarity nicely shows the periodicity of the reciprocal space: it does not matter whether we observe the band features in the 3rd, 4th or 6th repeated BZ. Differences occur only due to the influence of the photon momentum and the transition matrix elements, which depend on the final-state energy. The radial integrals change with decreasing period of the rapidly oscillating final-state wavefunction.

The similarity of the sections figures 4(c), (h) and (g) allows to draw an important conclusion. The clear identification of high-symmetry planes provides an absolute '*k*-ruler'. In the present case it proves that the approximation of the final state as free-electron like plane wave with adapted m_{eff}/m and $V_{\mathrm{o}}{}^{*}$ is very good. Between 300 and 1300 eV we do not find a significant energy dependence of m_{eff}/m and $V_{\mathrm{o}}{}^{*}$. Further, m_{eff}/m could depend on the direction of $\boldsymbol{k}_{\mathbf{f}}$. In the present data we do not find such a dependence. The *k*-field-of-view (radius 2 Å^{-1}) is only slightly larger than the BZ as visible in figure 4(a); BZ and momentum vectors are to scale. The final state momentum $\boldsymbol{k}_{\mathbf{f}}$ deviates only slightly from the (110)-direction perpendicular to the surface (vector $\boldsymbol{k}_{\mathbf{f}}^{\perp}$ in figure 4(a)).

4.2. Experimental results for the CDAD

In the present experiment we measured both photon helicities separately and derived the *CDAD signal* and *asymmetry* from these two individual measurements according to equation (1). No symmetry properties have been exploited because it was not *a-priori* clear which of them would persist when the photon momentum is non-negligible. This procedure is different from a previous low-energy experiment [15] with negligible photon momentum. In that work the dichroism asymmetry has been derived from a single measurement at fixed photon polarization, exploiting the symmetry properties of the setup.

Figure 5 shows measured intensity distributions being the sum of the RCP and LCP patterns (rows 1 and 3) and corresponding textures of the *CDAD* signal, see equation (1) (rows 2 and 4, respectively) for 14 photon energies between 306 and 1293 eV. The k_z-values of the sections, quantified in multiples of G_{110}, are given on top of the panels. The photon beam is oriented from top to bottom. There are four different mechanisms breaking the symmetry: (i) the photon momentum leads to a rigid downward shift of the complete pattern, increasing linearly with photon energy. (ii) The *CDAD* (i.e. the difference between RCP and LCP excitation) leads to a left-right asymmetry as visible in the reversed colors in the left and right half. (iii) The off-normal photon incidence gives rise to an additional contribution of the *LDAD* showing up as an up–down asymmetry. (iv) Local enhancement of intensity and *CDAD* signal can occur due to photoelectron diffraction. Enhancement factors of up to 5 have been observed in small regions of (E_{B}, $\boldsymbol{k}$) parameter space due to the action of the Laue equations on the outgoing photoelectron wave (for details, see [50]). In the following, we neglect this phenomenon because we believe that the normalization of the *CDAD* signal to the sum intensity removes most of the diffraction effect.

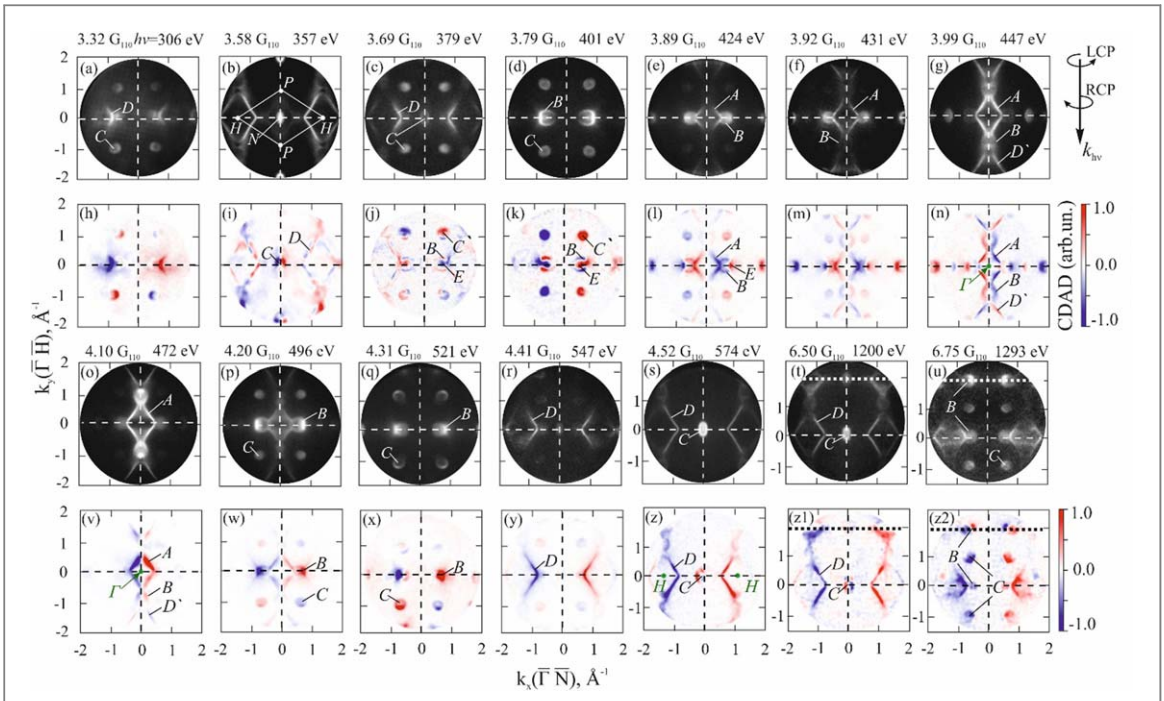

Figure 5. Measured momentum distributions (a)–(g), (o)–(u) and corresponding circular-dichroism textures (h)–(n), (v)–(z2) for the tungsten (110) surface at the Fermi level (energy isosurfaces at E_F) for 14 photon energies as stated above each panel. The momentum perpendicular to the surface (k_z) is quantified in multiples of the reciprocal lattice vector G_{110}. The circularly polarized photon beam impinges from top to bottom, see inset top right. The photon momentum $\boldsymbol{k}_{h\nu}^{\parallel}$ causes a rigid displacement of the patterns; dashed lines mark the center of the BZ, dotted lines in (t), (u), (z1), (z2) the center of the next BZ. The scale bar quantifies the CDAD.

Rows 2 and 4 reveal a surprisingly rich dichroism texture. The *CDAD signal* is color-coded, ranging between 1 (red) and −1 (blue), individually scaled for each panel. Corresponding *CDAD* asymmetries are very large (up to 90% with both polarities) and show a pronounced red–blue contrast and clear symmetry behavior. According to the scheme in figure 4(a) the electron distributions correspond to sections through the 3rd, 4th, 5th and 7th repeated BZ along k_z. The electron momentum increases with the root of the energy. A k-space distance of 0.25 G_{110} corresponds to an energy difference of 44 eV in the 4th BZ (see panels (a), (b)) and to 98 eV in the 7th BZ (panels (t), (u)).

In the intensity patterns, equivalent planes in different BZs look very similar, as seen by comparing the following groups of k-patterns in figure 5: 3.58, 4.52 and 6.50 G_{110} (b), (s), (t); 3.32, 3.69 and 6.75 G_{110} (a), (c), (u) and 3.79 and 4.31 G_{110} (d), (q). The only essential difference is the downward shift due to the photon momentum. However, the corresponding *CDAD* textures exhibit strong differences in size and sign of the *CDAD* signal. E.g. feature *D* exhibits a weak, bipolar *CDAD* at 3.58 G_{110} (i), whereas at 4.52 (z) and 6.50 G_{110} (z1) the same feature shows a rather pronounced *CDAD* with unipolar left-right asymmetry. These pronounced differences result from k_z being at, slightly above or below a mirror plane. The two mirror planes m and m' perpendicular to k_z are marked in figure 4(a). When going from 3.32 G_{110} (h) to 6.75 G_{110} (z2), the *CDAD*-asymmetry (red–blue contrast) of band feature *D* remains, whereas the asymmetry of features *C* is reversed. Likewise, the asymmetry of features *C* is reversed when going from 3.79 G_{110} (k) to 4.31 G_{110} (x). The maximum *CDAD* values occur at 3.32, 3.79 and 6.75 G_{110}, while the smallest occur at 3.58 and 3.99 G_{110}, i.e. close to the *N*–*H*–*P* plane and to the Γ-point.

The sign of the *CDAD* changes upon crossing the Γ-point, i.e. mirror plane m. This can be seen by comparing the *CDAD* texture of band feature *A* (inner diamond) at 3.89 and 3.92 G_{110} (l), (m) with the same feature at 4.1 G_{110} (v). For feature *C*, the ellipsoid-shaped hole pocket centered at the *N*-point we observe even several changes of sign, compare the *CDAD* of the lower left sphere: at 3.32 G_{110} it starts with positive sign (red). At 3.79 G_{110}, i.e. after crossing the first *N*–*H*–*P* plane (mirror plane m' in figure 4(a)) it has the opposite sign (blue). At 4.20 G_{110}, having crossed the 4th repeated Γ-point, the sign has changed again (red) and finally at 6.75 G_{110} it is blue, indicating that the general behavior of each repeated BZ is similar.

In order to analyze the *CDAD* patterns in more detail, we have to consider the symmetry of the crystal and the lifting of symmetries by the incoming photon beam. The bcc reciprocal lattice has high-symmetry planes, k_x–k_z, k_y–k_z and k_x–k_y. Due to the cubic symmetry, k_x, k_y and k_z pointing along the Γ–*N* direction in the bulk BZ are equivalent. However, the photon beam breaks this symmetry, see figure 1. In figure 5 the *CDAD* signal is

symmetric with respect to the horizontal plane but *anti-symmetric* with respect to the vertical plane. This anti-symmetry reflects the fact that the (axial) helicity vector is reversed upon this mirror reflection.

CDAD for non-magnetic systems requires a non-coplanar geometry of three vectors, the direction of photon impact $\boldsymbol{k_{h\nu}}$, electron momentum $\boldsymbol{k_e}$, and a third vector that represents a quantization axis for the initial electronic states. In previous studies at low energies, this vector was the surface normal or the molecular axis of an oriented molecule on the surface [8]. In the present case of photoexcitation in 3D k-space as described in figure 4(a) the surface normal is irrelevant and instead the bulk direction Γ–N takes the role of the quantization axis. If one expands the actual wave function in orbital wave functions close to a high symmetry point, the vector Γ–N naturally enters the calculation scheme in the same way as the surface normal did in the low-energy case.

4.3. Comparison with one-step photoemission calculations

A central goal of the present study was to elucidate whether one-step photoemission theory as described in section 2 is capable of calculating the *CDAD* in the soft-x-ray range. *CDAD* occurs due to interference terms between different final-state partial waves as illustrated in figure 2. It strongly depends on matrix elements and relative phases of interfering partial waves [13, 18]. Hence, *CDAD* is more sensitive to 'photoemission dynamics' (transition matrix elements and phases) than photoemission intensities.

Theoretical momentum slices at the Fermi energy have been calculated in the same photon-energy range as used in the experiment. In experiment and theory, the calibration of the k_z-scale was straightforward by searching for k-patterns characteristic for the position of high-symmetry planes. In particular, sections through the Γ-point and through the N–H–P plane (mirror planes m and m' in figure 4(a)) could easily be recognized by their pronounced characteristic features. The photon momentum was included in the theory. It turned out that in the calculation the photon energy was systematically ~3 eV higher than in the experiment. Similar differences between the experimental and theoretical photon energy had been found in other photoemission studies. The theoretical photon energy had to be shifted systematically by several eV to obtain a quantitative agreement with the corresponding experimental data. The reason is found in the fact that the LDA potential used as an electronic structure input is a ground-state quantity that describes especially for W the valence-band region very well, but for higher-lying unoccupied states it is only an approximation. As a consequence the energetic position of unoccupied conduction states is less accurate for higher photon energies. In a phenomenological view, the final state momentum is not exactly given by the free-electron dispersion. For tungsten we found an effective mass of $m_{\mathrm{eff}} = 1.07m$ in the experiment [42]. The inner potential is known to be energy dependent. Many-body effects are parametrized, leading to common shifts of all bands. The full consideration of electron correlations can lead to relative shifts, which might explain some quantitative discrepancies between theory and experiment (see below).

Figure 6 shows the comparison of experiment and theory for five selected photon energies. Here we show the *CDAD asymmetry* (see equation (1)). At first sight, the agreement between experiment and theory is not as good as in the low-energy region (see, e.g. [15, 51]). However the eye-catching differences essentially originate from just two facts: first, the Fermi-surface pockets B (electron-type), located at the six corners of the central octahedron A, appear much larger in theory than in experiment (compare figures 6(b), (c) with (g), (h)). This difference concerns the shape of the Fermi surface. Second, the ellipsoid-shaped hole-pockets C, centered at the N-points, appear rather weak in the calculated patterns (g), (j), whereas they are stronger in the experiment (b), (e). This difference concerns the intensity, the shape and position of the hole-pockets agree very well. In the N–H–P plane, hole pocket C appears in the center. Here theory and experiment agree quite well, as is the case for the diamond-shaped feature D resulting from the electron-like octahedron centered at the H-point (compare panels (a), (d) with (f), (i)). The same holds for the central octahedron A (c), (h).

Beyond these points, a few systematic differences remain. The hole ellipsoids C are visible in all calculated patterns (in fact, more momentum discs have been calculated than those shown in figure 6). They are completely absent in the experimental sections that do not intersect the hole pockets (figures 5(b), (e)–(g), (o), (r)–(t)). Likewise, the central octahedron A shows up weakly in the calculated patterns (figures 6(f), (g)), whereas in experiment it appears only in the cut through the central Γ–H–N plane (c), as expected for the tungsten Fermi surface, see figure 1(b). As mentioned in section 2, the calculations yielded some surface states, resulting from the finite number of atomic layers.

Besides these general differences, the calculated *CDAD* asymmetries show fair agreement with experiment. The signs agree for most band features. In particular the weak, 'bipolar' appearance of feature D in (k), (p) is very similar, indicating that these sections lie close to the N–H–P plane where the sign of the *CDAD* reverses. As mentioned above, the hole pockets C appear only weakly in theory, but in all panels the sign of their *CDAD* is identical to the experiment. However, it is remarkable that while theory predicts decreasing absolute values of the *CDAD* asymmetry with increasing photon energy, the experimental values stay surprisingly large even at the highest photon energies studied.

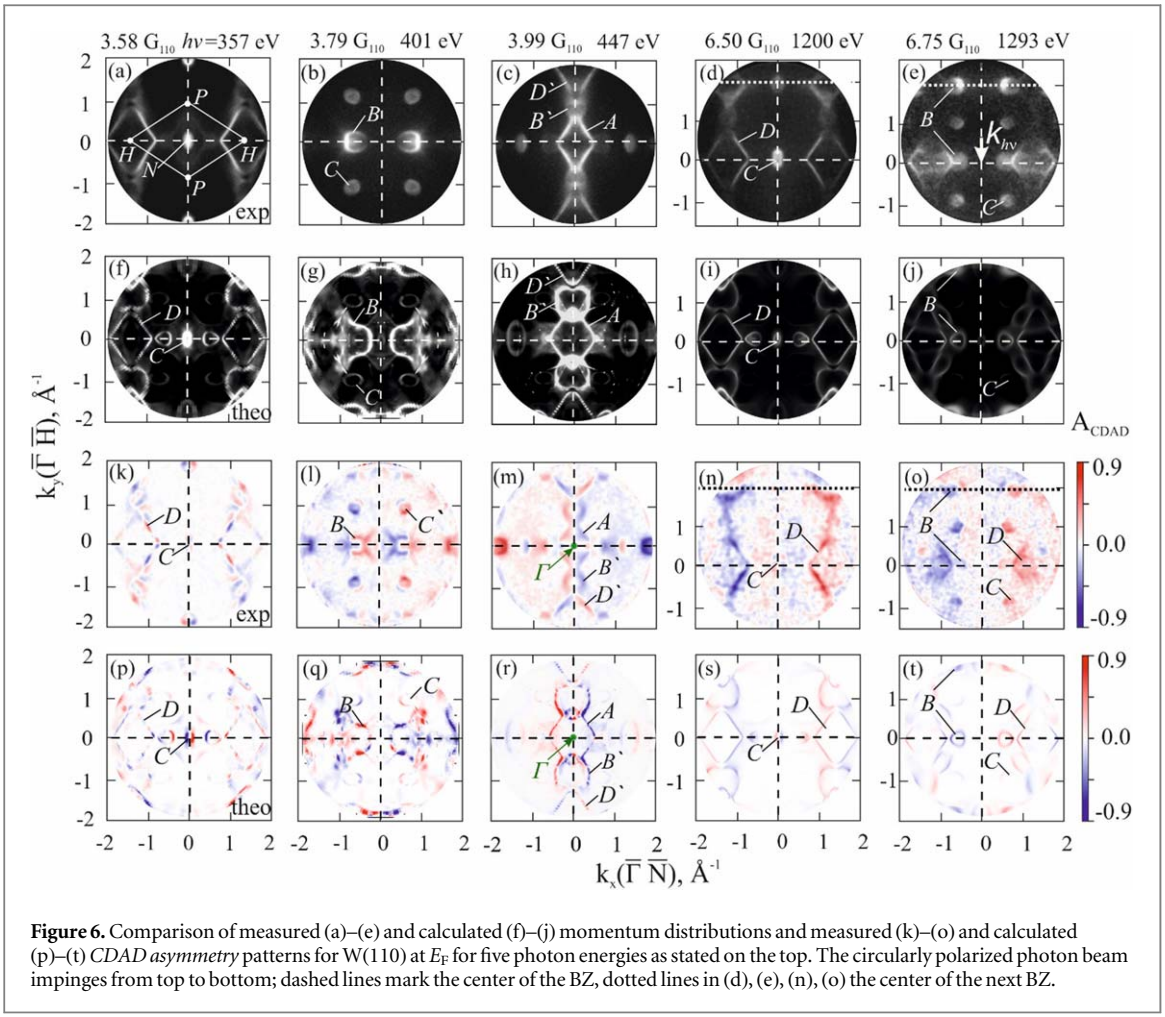

Figure 6. Comparison of measured (a)–(e) and calculated (f)–(j) momentum distributions and measured (k)–(o) and calculated (p)–(t) *CDAD asymmetry* patterns for W(110) at E_F for five photon energies as stated on the top. The circularly polarized photon beam impinges from top to bottom; dashed lines mark the center of the BZ, dotted lines in (d), (e), (n), (o) the center of the next BZ.

4.4. *CDAD* texture in 4D (E_B, $\boldsymbol{k}$) parameter space

In addition to the question whether a *CDAD* for valence bands exists at all in the soft-x-ray range and whether one-step theory can model this dichroism, the exploration of the 4D (E_B, $\boldsymbol{k}$)-texture of *CDAD* was a central goal of the present work. In particular, the symmetry behavior in full k-space is an interesting issue, because only 2D systems had been studied thus far. The crucial point here is that variation of the photon energy changes the momentum coordinate k_z perpendicular to the surface (as described in figure 4), but also the matrix element due to changing radial integrals. Moreover, the phase differences between different final-state partial waves tend to zero with increasing photon energy. All these effects influence the *CDAD* signal and thus its behavior was not *a-priori* clear.

For the study of the dichroism texture in the full bulk BZ all measured data sets $I_{RCP/LCP}$ (E_B, k_x, k_y) (for both orthogonal photon polarizations) for the 4th repeated BZ along k_z in a binding energy interval of 6 eV are concatenated, forming the two 4D-arrays $I_{RCP/LCP}$ (E_B, k_x, k_y, k_z). The curvature of the final-state spheres (see figure 4(a)) as well as a possible space-charge shift of the isosurfaces are corrected in this array (see [49]). Next, the *CDAD* asymmetry A_{CDAD} (E_B, $\boldsymbol{k}$) is determined voxel-by-voxel according to equation (1). This array contains the *CDAD* information in the complete BZ, including its dispersion with binding energy. In fact the 4D-arrays I and A_{CDAD} (equation 1) comprise the full information accessible in a (spin-integral) photoemission experiment, the so-called 'removal part' of the spectral function determined via the tomography-like mapping of the 4th repeated BZ as explained in figure 4.

There are several ways to visualize this 4D object in (E_B, $\boldsymbol{k}$) parameter space: (i) The projection of energy isosurfaces (E_B = const.) in k-space, 'decorated' with the *CDAD* asymmetry (figure 7 and movies in supplemental material is available online at stacks.iop.org/NJP/21/013017/mmedia). (ii) 'k_z-scan movies' visualizing the tomographic analysis of the BZ (k_z-scans for 3 values of E_B are shown in the supplemental material). (iii) The E_B-versus-$k_{||}$ representation of the dispersing bands with their *CDAD* asymmetry, visualizing the binding energy dependence of *CDAD* along one selected direction in k-space (examples in figure 8). Figure 7 shows the central experimental result of this paper, the dichroism texture on three selected energy isosurfaces (at E_B = 0, 1.5 and 2 eV) from a total of ~100 resolved energies. For improved clarity, these k-space objects are shown as movies in the supplementary material. The *CDAD* is quantified by the red–grey–blue color bar. Red

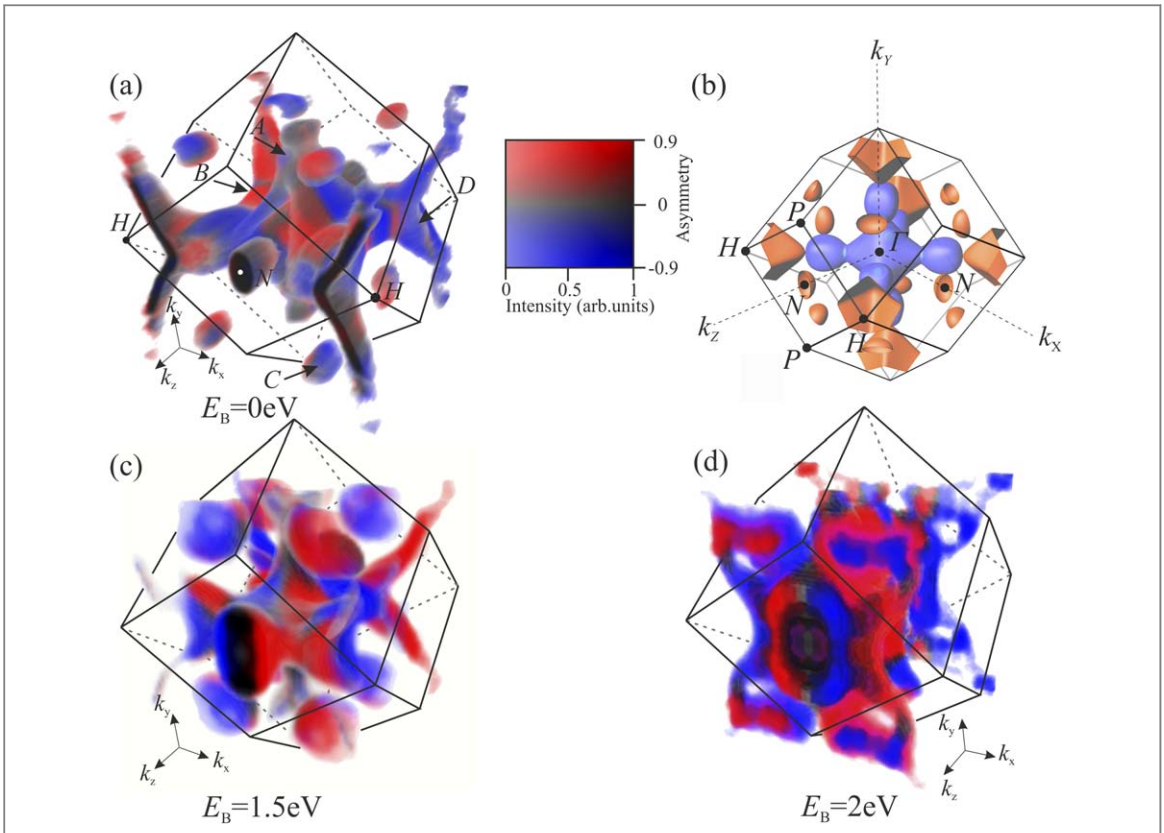

Figure 7. (a) Fermi surface with overlaid *CDAD asymmetry*, quantified by the color bar. Red and blue correspond to positive and negative *CDAD*, respectively, and grey denotes intensity but zero *CDAD*. (b) Theoretical Fermi surface, with blue and red denoting electron and hole sheets (from [31, 32]). (c) and (d) Isosurfaces with overlaid *CDAD asymmetry* for binding energies of 1.5 eV and 2 eV, respectively. These *CDAD* textures have been projected from the 4D-arrays $I_{RCP/LCP}$ (E_B, $\boldsymbol{k}$) by calculating voxel-by-voxel the asymmetry defined in equation (1). Movies showing the full 3D texture can be found in the supplemental material.

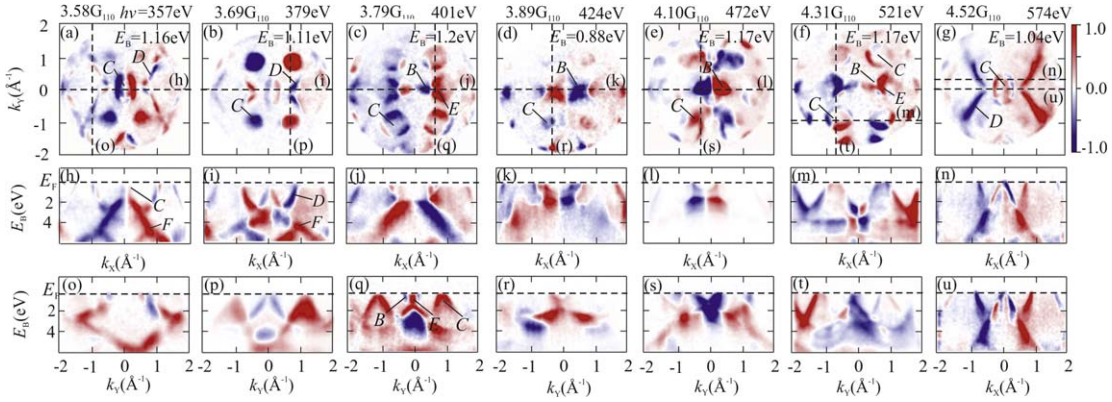

Figure 8. Dispersion behavior of the *CDAD signal* for several photon energies. First row: k_X–k_Y slices of the *CDAD* signal for binding energies E_B below the Fermi energy, as stated in the panels. Second and third rows: E_B-versus-k_X and E_B-versus-k_Y *CDAD* sections along the dashed lines in panels (a)–(g) along k_X (h)–(n), (u) and parallel to k_Y (o)–(t). The scale bar quantifies the CDAD.

and blue denote positive and negative *CDAD* (red denotes higher intensity with RCP excitation), while the shade of grey marks unpolarized intensity. In this way, pockets and sheets are visible on the isosurface even if the *CDAD* vanishes.

We discuss the basics of the *CDAD* texture in the 4D parameter space, starting with the example of the ellipsoid-shaped hole pockets *C*, centered at the 12 *N*-points. These pockets show the maximum asymmetry up to 90%. Due to the cubic symmetry (O_h), the wavefunctions at all *N*-points are identical. Only the quantization axes for the angular momenta are different, because the vector Γ–*N* has 12 possible directions. In the ground-state all 12 are equivalent. However, the photon beam breaks this symmetry. For the magnitude and sign of the *CDAD*, we have to consider each individual Γ–*N* direction separately. In this respect, the behavior of the *CDAD*

in bulk photoemission differs from previous work at low energies [6, 8, 13], where only the surface normal was considered as relevant quantization direction.

Figure 7 reveals the symmetry properties of the *CDAD* with respect to the mirror operations. The *anti-symmetry with respect to the k_y–k_z plane* reflects the fact that the (axial) helicity vector is reversed upon this mirror reflection. Conversely, the *k_x–k_z symmetry* reflects that the helicity is retained upon this mirror operation. These symmetry properties are identical to the low-energy case. However, the third property, i.e. the *anti-symmetry with respect to mirror planes parallel to k_x–k_y* has not been observed before because k_z could not be varied in previous low-energy experiments. Due to this anti-symmetry, the *CDAD* changes its sign when k_z crosses a mirror plane perpendicular to k_z (denoted as m and m' in figure 4). These are the Γ–H–N plane (m) running through the center of the BZ and the N–H–P plane (m') forming the boundary to the next BZ. We attribute this behavior to the mirror anti-symmetry of the odd partial waves in the expansion of the corresponding initial-state wavefunction. The translational periodicity of BZs (figure 4) demands that the orbital parts of the wavefunctions are periodic as well. Hence, the relative phase of the lobes of all partial waves with odd parity switch when crossing a mirror plane (with the exception that the lobe lies in the mirror plane). This switching is invisible in the intensity patterns, because the symmetry predicts a complete cancellation of the *CDAD* for the sum of the intensities for circular left and right polarization. The *CDAD,* however, is affected by this phase switch at the mirror planes m and m' because it is sensitive to the relative phases of wavefunctions [6, 8, 13]. This novel symmetry property suggests that the sign change of *CDAD* can be utilized to find mirror planes and high-symmetry points in direct transitions in periodic k-space as depicted in figure 4. Note that the size of the *CDAD* signal is not identical in subsequent repeated BZs because the radial matrix elements depend on photon energy.

Figure 8 shows *CDAD*-dispersions along k_x and k_y at seven selected values of k_z (given on top). The first row presents constant-energy sections at higher binding energies $E_B \neq 0$. Rows 2 and 3 show E_B–$k_{||}$ sections along the dashed lines in panels (a)–(g). The anti-symmetry with respect to the k_y–k_z mirror plane is clearly visible in panels (h)–(n), (u) and the *CDAD* shows a pronounced dispersion. At higher binding energies, several features appear with a substructure that was not visible in the intensity patterns and sections at the Fermi energy. At 3.69 G_{110} the diamond-shaped band D (centered at the H-point) exhibits intensity inside of the diamond that has the opposite sign of *CDAD,* see red color in top right part of figure 8(i). With increasing binding energy, the substructure vanishes, and band D disperses outwards and intersects with the oval feature C centered on the N-point. Moreover, a new band F appears in the E_B-versus-k_X sections (h), (i) that is an extension of band C (figure 5(i)) and shows a very pronounced *CDAD*. A further interesting substructure E appears inside of band B as indicated in figures 8(c), (q) and figures 5(j)–(l). This second Fermi surface pocket inside of pocket B has previously been discussed in the early theoretical work of Christensen and Feuerbacher [52].

At $k_z = 4.31\ G_{110}$ features C and B-spheres exhibit substructures (figures 8(c), (q), (f), (m)). In some cases, the bipolar *CDAD* is even more pronounced at higher binding energies, for example, for band B at $E_B > 3.5$ eV (figure 8(m)). Figures 8(a), (g) show the dichroic behavior in cuts corresponding to similar positions in two adjacent (4th and 5th) BZs. The *CDAD* and its dependence on binding energy for those two cases are significantly different at high E_B. The *CDAD* has a rich bipolar structure at $k_z = 4.52\ G_{110}$ that corresponds to the 5th repeated BZ (see figure 7(o)). In particular, feature C has a double bipolar structure of the *CDAD* sign at $E_B = 2$ eV. The differences between (h), (u) are remarkable, in particular concerning the sign of the *CDAD*.

In addition to the *CDAD*, the E_B-versus-k_Y cuts also reveal a sizeable *LDAD* effect due to the tilted direction of photon incidence (see end of section 2.1). Most features have significantly different dichroism values in the upper and lower half (third row of figure 8).

Not only the sign but also the value of the *CDAD* is different in various points of the BZ (figure 8). The Γ-point (photon energy 447 eV, $k_Z \approx 3.99\ G_{110}$) shows the smallest value of the *CDAD* (35%) while the extrema of 85%–90% are observed at 379 eV ($3.69\ G_{110}$) and 521 eV ($4.31\ G_{110}$). In other words, with moving away from the Γ-point in both directions along k_Z the *CDAD* generally increases. Thus, at energies of 424 eV ($3.89\ G_{110}$) and 472 eV ($4.10\ G_{110}$) on the way from the Γ-point to N–H–P planes the *CDAD* value is at maximum ~55% with the opposite sign (see figures 8 (a), (b)). Sections E_B-versus-k_x at $k_y = 0$ show the same value of the *CDAD* up to $E_B \approx 2$ eV (see figures 8 (c), (d)). These sections and also the sections E_B-versus-k_y (see figures 8 (e), (f)) at $k_x = 0.3$ Å^{-1} indicate how the sign of the *CDAD* changes while passing the Γ-point. For instance, identical features have an opposite color at symmetrical points in the BZ.

As mentioned above the effect of the photon momentum is significant and has to be taken into account in the data evaluation (see [42]). However, we did not observe any hints on a recoil effect as observed and discussed for light elements [28].

Figure 6 (third row) and figure 8 (first row) show that sizeable *CDAD* is present at practically all photon energies studied. The *CDAD* asymmetry is reduced only when the final state sphere crosses a high symmetry plane (like in figure 6 (k)). Given a proper calibration (like in figure 8) the degree of circular polarization can be quantitatively determined from the *CDAD asymmetries* in a wide photon energy range. The method should be very powerful in validating the circular polarization as function of the undulator phase shift.

5. Summary and conclusion

We have investigated *CDAD* for the *d*-band complex of tungsten in the soft-x-ray spectral region between $h\nu = 300$ and 1300 eV. The experiment was performed at the circularly polarized high-brilliance beamline P04 of the storage ring PETRA III (DESY, Hamburg). Due to the large photoelectron escape depth, the observed signal originates mainly from transitions in the bulk of the material. Hence, the size and symmetry properties of the *CDAD* could, for the first time, be studied in the full 3D bulk BZ.

All previous *CDAD* experiments have studied electronic systems in 2D (surfaces, adsorbates) or even 1D (e.g. oriented linear molecules). Given a fixed quantization axis (mostly the surface normal), size and sign of the *CDAD* was determined by the dipole matrix elements and relative phases [8, 13]. Prior to the present experiment it was not clear whether a *CDAD* effect can exist in bulk transitions in the soft-x-ray range. The bulk electronic states are governed by the symmetry group of the crystal and previous theories could not predict the existence and the symmetry properties of a possible *CDAD* in 3D *k*-space.

Using photoelectron momentum microscopy, we performed a tomographic mapping in a wide range of k_z between the 3rd and 7th repeated BZ in order to observe the variation of the *CDAD* signal across several BZs. The 4th BZ was mapped in detail by varying the photon energy between 357 and 574 eV in small steps, corresponding to increments of $\Delta k_z = 0.1$ Å^{-1}. Exploiting ToF parallel energy recording, the *helicity-dependent spectral functions* $I_{\mathrm{RCP,LCP}}(E_B, k_x, k_y)$ were measured at each photon energy. The derivation (voxel-by-voxel) of their difference $I_{\mathrm{RCP}} - I_{\mathrm{LCP}}$ yields the *CDAD signal*, and division by the sum $I = I_{\mathrm{RCP}} + I_{\mathrm{LCP}}$ then yields the *CDAD asymmetry* (in complete analogy with XMCD [2–4]). By concatenating all arrays taken at different photon energies, we finally arrive at the *circular dichroism texture* $A_{CDAD}(E_B, \boldsymbol{k})$ in 4D parameter space, the central object of the present paper. The 4D-arrays I and A_{CDAD} contain the full information accessible in a (spin-integral) photoemission experiment. $A_{CDAD}(E_B, \boldsymbol{k})$ was visualized by *energy isosurfaces* ($E_B = $ const.) in 3D *k*-space, 'decorated' by the color-coded *CDAD* asymmetry (perspective views in figure 7; movies in supplemental material showing the full 3D texture). Of particular interest is the isosurface at the Fermi level, but the *CDAD* texture for all other binding energies can be projected from the 4D array as well. k_z-scan movies (see supplemental material) visualize the tomographic analysis of the BZ. Sections with two momentum components kept constant yielded the *CDAD dispersion behavior* E_B-versus-k_x or k_y (figure 8).

Large dichroism asymmetries of up to 90% have been observed throughout the energy range studied. The asymmetry shows a pronounced dependence on photon energy and on all three components of the *k*-vector. This result is surprising because in its quantum-mechanical description, *CDAD* depends on terms containing the sine of partial wave phase-shift differences which tend to zero with increasing photon energy [29]. Apparently, additional phase differences of partial waves occur due to diffraction of the photoelectron wave on neighboring atoms.

In order to elucidate the behavior in 3D *k*-space in detail, we have studied the *CDAD*-patterns at equivalent k_z-positions in three different BZs (4th, 5th and 7th) in the periodic zone scheme, corresponding to photon energies of 357, 574 and 1300 eV, respectively. These results uncovered the following *symmetry rules of CDAD* in 3D *k*-space: the anti-symmetric behavior with respect to the plane of incidence (known for 2D systems [13]) persists in the 3D case if this plane is a mirror plane of the crystal. A central new result is the symmetry behavior with respect to mirror planes perpendicular to k_z, a symmetry element that did not exist in the 2D systems studied previously. *CDAD* changes its sign whenever such a mirror plane (e.g. m and m' in figure 4) is crossed by the direct transition in the periodic scheme of BZs (figure 7). This can be understood in terms of a 'switching' of the relevant quantization axis upon each crossing of a mirror plane. The origin of this anti-symmetry of *CDAD* lies in the subtle effect that the relative phase of the lobes of initial partial-wave angular wavefunctions with odd parity switch when crossing a mirror plane. This change of the relative phases cancels out in the intensity patterns (given by squared wavefunctions) but is visible in the *CDAD* which contains additional interference terms [6, 13, 16]. Hence, *CDAD* provides a powerful tool to identify mirror planes of the bulk BZ in photoemission experiments.

One-step photoemission calculations for various photon energies in the same spectral range show fair overall agreement with the measured results. The calculation reveals the reason for the variation of *CDAD* with photon energy: with increasing excitation energy, the wavelength of the free-electron-like final state varies strongly (between $\lambda \approx 4$ and 1 Å for kinetic energies between 300 and 1300 eV), thus causing substantial changes in the radial integrals of the dipole matrix element. Theory yields sharp band features persisting up to photon energies of almost 1400 eV (figure 3). The band patterns show significant changes when the photon energy is increased by only 5 eV, corresponding to an increment of k_z by 0.01 Å^{-1}. Comparison of theoretical and experimental results for several photon energies shows good agreement in the sign and magnitude of *CDAD* for the various band features. Differences occur in details of the shape of the Fermi surface and in the presence of surface resonances which are absent in the experimental data.

The present experiment has shown that large *CDAD* asymmetries persist in bulk photoemission in the soft-x-ray range, described in terms of direct transitions to free-electron-like final states (as depicted in figure 4). *CDAD* shows a rich texture in 4D (E_B, $\boldsymbol{k}$) parameter space. The variation of photon energy changes on the one hand the momentum coordinate perpendicular to the surface and on the other hand also the radial integrals of the transition matrix elements. Both effects influence the *CDAD* signal. Due to the previously unobserved mirror-plane anti-symmetry, *CDAD* allows an unambiguous identification of high-symmetry planes in direct transitions in the periodic zone scheme. It further reveals the dominant orbital symmetry (parity) of bands near high-symmetry points. The high degrees of asymmetry (up to 90%) can be exploited as a novel circular polarimeter for soft, tender (and possibly hard) x-rays.

Acknowledgments

We thank the Petra III staff for the excellent support and C Tusche (Forschungszentrum Jülich) for fruitful discussions. The project is funded by BMBF (05K16UM1, 05K13GU3) and DFG (Transregio SFB Tr173 Spin +X, RE1469/13-1 and SFB 925/B2). JM thanks for support from CEDAMNF (CZ.02.1.01/0.0/0.0/15_003/0000358) of Czech Ministerium MSMT.

Note added in proof

Meanwhile similar experiments have been performed in the hard x-ray range at the new beamline P22 of PETRA III. Momentum distributions recorded at photon energies up to 6 keV [53] reveal sharp band features of similar quality as in the soft x-ray range.

ORCID iDs

O Fedchenko https://orcid.org/0000-0002-6159-7934
C-H Min https://orcid.org/0000-0002-2732-8773
Y Acremann https://orcid.org/0000-0002-4109-3544

References

[1] Hecht E and Zajac A 1974 *Optics* (Reading, MA: Addison-Wesley) p 565
[2] Schütz G, Wagner W, Wilhelm W and Kienle P 1987 Absorption of circularly polarized x rays in iron *Phys. Rev. Lett.* **58** 737
[3] van Der Laan G and Thole B T 1994 Classification for angle dependent polarized photoemission spectra using magnetic moments analysis *Solid State Commun.* **92** 427
[4] Stöhr J 1999 *J. Magn. Magn. Mater.* **200** 470
[5] Ritchie B 1975 *Phys. Rev.* A **I2** 567
[6] Cherepkov N A 1982 Circular dichroism of molecules in the continuous absorption region *Chem. Phys. Lett.* **87** 344
Cherepkov N A and Schönhense G 1993 Linear dichroism in photoemission from Oriented molecules *Europhys. Lett.* **24** 79
[7] Lee C M 1974 Spin polarization and angular distribution of photoelectrons in the Jacob-Wick helicity formalism. Application to autoionization resonances *Phys. Rev.* A **10** 1598
[8] Westphal C, Bansmann J, Getzlaff M and Schönhense G 1989 Circular dichroism in the angular distribution of photoelectrons from oriented CO molecules *Phys. Rev. Lett.* **63** 151
[9] Daimon H, Nakatani T, Imada S and Suga S 1995 Circular dichroism from non-chiral and non-magnetic materials observed with display-type mirror analyzer *J. Electron Spectrosc. Relat. Phenom.* **76** 55
[10] Venturini F, Minár J, Braun J, Ebert H and Brookes N B 2008 Soft x-ray angle-resolved photoemission spectroscopy on Ag(001): band mapping, photon momentum effects and circular dichroism *Phys. Rev.* B **77** 045126
[11] Wießner M, Hauschild D, Sauer C, Feyer V, Schöll A and Reinert F 2014 Complete determination of molecular orbitals by measurement of phase symmetry and electron density *Nat. Commun.* **5** 4156
[12] Bentmann H, Maaß H, Krasovskii E E, Peixoto T R F, Seibel C, Leandersson M, Balasubramanian T and Reinert F 2017 Strong linear dichroism in spin-polarized photoemission from spin–orbit-coupled surface states *Phys. Rev. Lett.* **119** 106401
[13] Schönhense G 1990 Circular dichroism and spin polarization in photoemission from adsorbates and non-magnetic solids *Phys. Scr.* **T31** 255
[14] Grimme S, Peyerimhoff S D, Bartram S, Vögtle F, Breest A and Hormes J 1993 Experimental and theoretical study of the circular dichroism spectra of oxa-[2,2]metacyclophane and thia-[2.2]metacyclophane *Chem. Phys. Lett.* **213** 32
[15] Chernov S V *et al* 2015 Anomalous d-like surface resonances on Mo(110) analyzed by time-of-flight momentum microscopy *Ultramicroscopy* **159** 453
[16] Schönhense G, Westphal C, Bansmann J and Getzlaff M 1992 Circular dichroism in photoemission from nonmagnetic low-z solids: a conspicuous effect of the photon spin *Europhys. Lett.* **17** 727
[17] Schönhense G, Westphal C, Bansmann J, Getzlaff M, Noffke J and Fritsche L 1991 Circular dichroism in photoemission from surfaces *Surf. Sci.* **251** 132
[18] Bansmann J, Ostertag C, Schönhense G, Fegel F, Westphal C, Getzlaff M, Schafers F and Peterson H 1992 Circular dichroism in x-ray photoemission from core levels of non-magnetic species *Phys. Rev.* B **46** 13496

[19] Oelsner A, Ziethen C, Fecher G H and Schönhense G 2002 Imaging of dichroism in photo-emission electron microscopy at nonmagnetic materials using circularly polarized soft x-rays *Surf. Rev. Lett.* **09** 509
[20] Fecher G H 1995 The solid surface as origin of circular dichroism in the angular distribution of photoelectrons from spherical states of adsorbates *Europhys. Lett.* **29** 605
[21] Getzlaff M, Bode M and Wiesendanger R 1998 Determination of radial matrix elements and phase shifts in photoemission with a rotatable electric-field vector *Phys. Rev.* B **58** 9681
[22] Strocov V N 2003 Intrinsic accuracy in 3-dimensional photoemission band mapping *J. Electron Spectrosc. Relat. Phenom.* **130** 00054–9
[23] Schneider C M, Venus D and Kirschner J 1992 Strong x-ray magnetic circular dichroism in a 'forbidden geometry' observed via photoemission *Phys. Rev.* B **45** 5041
[24] Suga S 2001 Extremely high quality soft x-ray beam line BL25SU of Spring-8: instrumentation and research activities *Nucl. Instrum. Methods Phys. Res.* A **467–468** 1388
[25] Gray A X *et al* 2011 Probing bulk electronic structure with hard x-ray angle-resolved photoemission *Nat. Mater.* **10** 759
[26] Suga S and Tusche C 2015 Photoelectron spectroscopy in a wide $h\nu$ region from 6 eV to 8 keV with full momentum and spin resolution *J. Electron Spectrosc. Relat. Phenom.* **200** 119–42
[27] Hüfner S 2003 *Photoelectron Spectroscopy— Principles and Applications* (Berlin: Springer)
[28] Suga S and Sekiyama A 2014 *Photoelectron Spectroscopy. Bulk and Surface Electronic Structures* (Berlin: Springer)
[29] Manson S T 1969 Dependence of the phase shift on energy and atomic number for electron scattering by atomic fields *Phys. Rev.* **182** 97 and private communication
[30] Fecher G H *et al* 1999 Dichroism in angular resolved VUV-photoemission from the (0001) surfaces of thin Gd and Nd films epitaxially grown on W(110) *Eur. Phys.* B **11** 161–75
[31] Mattheiss L F 1965 Fermi surface in tungsten *Phys. Rev.* **139** 1893
[32] Choi D, Kim C S, Naveh D, Chung S, Warren A P, Nuhfer N T, Toney M F, Coffey K R and Barmak K 2012 Electron mean free path of tungsten and the electrical resistivity of epitaxial (110) tungsten films *Phys. Rev.* B **86** 045432
[33] Goldberg S M, Fadley C S and Kono S 1981 *J. Electron Spectrosc. Relat. Phenom.* **21** 285
[34] Schönhense G 1990 Spin-dependent effects in photoemission *Vacuum* **41** 506
[35] Fecher G H, Kuznetsov V V, Cherepkov N A and Schönhense G 2002 Influence of the symmetry on the circular dichroism in angular resolved core-level photoemission *J. Electron Spectrosc. Relat. Phenom.* **122** 157
[36] Minár J, Braun J and Ebert H 2013 Recent developments in the theory of HARPES *J. Electron Spectrosc. Relat. Phenom.* **190** 159
[37] Minár J, Braun J, Mankovsky S and Ebert H 2011 Calculation of angle-resolved photoemission spectra within the one-step model of photoemission—recent developments *J. Electron Spectrosc. Relat. Phenom.* **184** 91
[38] Plucinski L, Minár J, Sell B C, Braun J, Ebert H, Schneider C M and Fadley C S 2008 Band mapping in higher-energy x-ray photoemission: phonon effects and comparison to one-step theory *Phys. Rev.* B **78** 035108
[39] Tanuma S, Powell C J and Penn D R 2011 *Surf. Interface Anal.* **43** 689
[40] Fadley C S 2005 X-ray photoelectron spectroscopy and diffraction in the hard x-ray regime: fundamental considerations and future possibilities *Nucl. Instrum. Methods Phys. Res.* A **547** 24
[41] Schmid B *et al* 2004 Hard x-ray photoemission on ferromagnetic MnAs clusters in a gaAs matrix *DESY Rep.* **1** 41
[42] Medjanik K *et al* 2017 Direct 3D mapping of the fermi surface and fermi velocity *Nat. Mater.* **16** 615–21
[43] Schönhense G, Medjanik K and Elmers H-J 2015 Space-, time- and spin-resolved photoemission *J. Electron Spectrosc. Relat. Phenom.* **200** 94
[44] Viefhaus J, Scholz F, Deinert S, Glaser L, Ilchen M, Seltmann J, Walter P and Siewert F 2013 The variable polarization XUV beamline P04 at PETRAIII: optics, mechanics and their performance *Nucl. Instrum. Methods* **710** 151
[45] Tusche C, Krasyuk A and Kirschner J 2015 Spin resolved band structure imaging with a high resolution momentum microscope *Ultramicroscopy* **159** 520
[46] Oelsner A, Rohmer M, Schneider C, Bayer D, Schönhense G and Aeschlimann M 2010 Time- and energy resolved photoemission electron microscopy-imaging of photoelectron time-of-flight analysis by means of pulsed excitations *J. Electron Spectrosc. Relat. Phenom.* **178–179** 317
[47] Bauer E 1962 *Electron Microscopy.* vol 1 Sydney S and Breese J (New York: Academic) p 0–11
[48] Telieps W and Bauer E 1985 An analytical reflection and emission UHV surface electron microscope *Ultramicroscopy* **17** 57–65
[49] Schönhense B *et al* 2018 Multidimensional photoemission spectroscopy—the space-charge limit *New J. Phys.* **20** 033004
[50] Schönhense G, Medjanik K, Babenkov S, Vasilyev D, Ellguth M, Fedchenko O, Chernov S, Schönhense B and Elmers H J 2018 Momentum-transfer model of valence-band photoelectron diffraction arXiv:1806.05871 [cond-mat.mtrl-sci]
[51] Schönhense G *et al* 2017 Spin-filtered time-of-flight k-space microscopy of Ir—towards the 'complete' photoemission experiment *Ultramicroscopy* **183** 19–29
[52] Christensen N E and Feuerbacher B 1974 Volume and surface photoemission from tungsten: I. Calculation of band structure and emission spectra *Phys. Rev.* B **10** 23492357
[53] Medjanik K *et al* 2018 Breakthrough in HAXPES performance combining full-field k-imaging with time-of-flight recording arXiv:1810.11366